at community and ecosystem levels. Calcification versus saturation experiments cited here were conducted over days to weeks. Whether individual reef-building species display an acute versus chronic response to saturation state or whether they can adapt to more gradual changes in carbonate chemistry is unknown. Possible mitigative physiological effects, such as CO_2 fertilization of calcareous algae or the symbiotic algae within coral tissues, are addressed elsewhere (*12*). The geological record offers no evidence of either adaptation or mitigative affects; nonetheless, these considerations are important when the effects of global change on photosynthetic and calcifying organisms are being weighed.

Given the decrease in average tropical Ω-arag from 4.6 to 4.0 over the past century, net calcification has probably already decreased on some reefs. We may be able to detect such changes in coral records through either coral calcification or stable isotope records. For example, $\delta^{13}C$ and $\delta^{18}O$ in several foraminiferans correlate strongly with carbonate saturation state (*18*). Although reduced calcification decreases the ocean-atmospheric CO_2 flux, this effect will be small because CO_2 evasion from reef calcification is only about 1% that of present-day fossil fuel emissions (*19*).

The possibly dire consequences of reduced reef calcification warrant a much closer look at the biogeochemistry of shallow water carbonate secretors. Better quantification of the calcification-saturation relationship, through laboratory and field studies, and examination of geologic records are needed, as is a mechanistic understanding of calcification physiology in corals and algae (*12*). This analysis has focused on coral reef calcification, but other calcifying marine ecosystems (both neritic and open ocean) may share similar risks.

References and Notes

1. J. T. Houghton *et al.*, *Climate Change 1995. The Science of Climate Change* (Cambridge Univ. Press, Cambridge, 1996).
2. H. Y. Inoue, M. Ishii, H. Matsueda, M. Ahoyama, I. Asanuma, *Geophys. Res. Lett.* **23**, 1781 (1996); C. L. Sabine, D. W. R. Wallace, F. J. Millero, *Eos* **78**, 49 (1997); N. Gruber, *Global Biogeochem. Cycles* **12**, 165 (1998).
3. T. Takahashi *et al.*, *Proc. Natl. Acad. Sci. U.S.A.* **94**, 8292 (1997).
4. S. V. Smith and R. W. Buddemeier, *Annu. Rev. Ecol. Syst.* **23**, 89 (1992); R. W. Buddemeier, *Bull. Inst. Oceanogr (Monaco)* **13**, 119 (1994); ______ and D. G. Fautin, *ibid.* **14**, 23 (1996); *ibid.*, p. 33.
5. P. A. Sandberg, in *The Carbon Cycle and Atmospheric CO_2: Natural Variations Archean to Present, American Geophysical Union Monograph 32*, E. T. Sundquist and W. S. Broecker, Eds. (American Geophysical Union, Washington, DC, 1985), pp. 585–594; P. Sandberg, in *Carbonate Cements*, Society of Economic Paleontologists and Mineralogists (SEPM) Special Publication 36, N. Schneidermann and P. M. Harris, Eds. (SEPM, Tulsa, OK, 1985), pp. 33–57.
6. B. N. Opdyke and B. H. Wilkinson, *Am. J. Sci.* **293**, 217 (1993); *Palaeogeogr. Palaeoclim. Palaeoecol.* **78**, 135 (1990).
7. J. Kleypas, J. McManus, L. Meñez, *Am. Zool.* **39**, 146 (1999).
8. W. S. Broecker and T. Takahashi, *J. Geophys. Res.* **71**, 1575 (1966); S. V. Smith and R. Pesret, *Pac. Sci.* **28**, 225 (1974).
9. C. J. Crossland, *Proc. 6th Int. Coral Reef Symp.* **1**, 221 (1988); J. E. N. Veron, *A Biogeographic Database of Hermatypic Corals* (Australian Institute of Marine Science Monograph Series 10, Townsville, Australia, 1993) (although Crossland attributed lighter calcification to low temperatures or low light, or both).
10. A. K. A. Behairy and M. K. El-Sayed, *Mar. Geol.* **58**, 443 (1984).
11. J. Cortés, *Coral Reefs* **16**, S39 (1997).
12. Gattuso *et al.* [J.-P. Gattuso, D. Allemand, M. Frankignoulle, *Am. Zool.* **39**, 160 (1999)] compiled data on two temperate coralline algae species, *Bossiela orbigniana* [A. D. Smith and A. A. Roth, *Mar. Biol.* **52**, 217 (1979)] and *Corallina pilulifera* [K. Gao *et al.*, *ibid.* **177**, 129 (1973)]; two tropical coralline algae species, *Amphiroa foliacea* [M. A. Borowitzka, *ibid.* **62**, 17 (1981)] and *Porolithon gardineri* [C. R. Agegian, thesis, University of Hawaii (1985)]; and two scleractinian corals, *Stylophora pistillata* and *Porites compressa* (F. Marubini and N. J. Atkinson, personal communication to Gattuso *et al.*). Our analysis excluded *P. compressa* (calcification response to saturation state was highest of the above species but included only two data points) and temperate species.
13. C. Langdon, T. Takahashi, T. McConnaughey, H. Anderson, H. West, paper presented at the Society for Integrative and Comparative Biology Annual Meeting, Boston, MA, January 1998. A 40% drop in calcification under double CO_2 conditions was found. Saturation state was altered by manipulating $[CO_3^{2-}]$ by adding sodium carbonate and sodium bicarbonate without changing pH.
14. Atmospheric $P\text{CO}_2$ and temperature were adjusted according to projections of IPCC, IS95a (*1*). Surface $P\text{CO}_2$ was adjusted by using sea-air $P\text{CO}_2$ differences of Takahashi *et al.* (*3*). Total alkalinity (TA) was determined as follows: TA = NTA × (salinity/35), where NTA (normalized total alkalinity) = 2306 μEq kg^{-1} [W. S. Broecker and T. H. Peng, *Global Biogeochem. Cycles* **3**, 215 (1989)]. SST and salinity were from Levitus [S. Levitus, *NOAA Professional Papers*, vol. 13 (Government Printing Office, Washington, DC, 1994)], and PO_4 and SiO_2 concentrations were from Levitus *et al.* [S. Levitus, M. E. Conkright, J. L. Reid, R. G. Najjar, A. Mantyla, *Prog. Oceanogr.* **31**, 245 (1993)]. $[CO_3^{2-}]$ was calculated by using standard constants for CO_2 solubility in water (K_0) [R. F. Weiss, *Mar. Chem.* **2**, 203 (1974)] and stoichiometric constants for ionization of carbonic acid in seawater (K_1 and K_2) [F. J. Millero, *Geochim. Cosmochim. Acta* **59**, 661 (1995)]. Phosphate and silicate were maintained at present-day levels. Ω-arag was calculated by using K'_{sp} adjusted for temperature and salinity [A. Mucci, *Am. J. Sci.* **283**, 780 (1983)]. All calculations were done on a 1° grid.
15. E. Maier-Reimer and K. Hasselmann, *Clim. Dyn.* **2**, 63 (1987); E. Maier-Reimer, *Global Biogeochem. Cycles* **7**, 645 (1993).
16. Model atmosphere $P\text{CO}_2$ was held to 278 μatm for 1750 years while ocean chemistry adjusted to this steady state. Beginning in 1750, $P\text{CO}_2$atm was increased, following historical levels to the present. Future $P\text{CO}_2$ to the year 2200 was taken from the projection of Kheshgi *et al.* [H. S. Kheshgi, A. K. Jain, D. J. Wuebbles, *Clim. Change* **33**, 31 (1996)]. Sea-surface temperature was continuously adjusted according to $\Delta T = \ln(P\text{CO}_2/P\text{CO}_{2(\text{init})}) \times \Delta T_{2x}$, where $\Delta T_{2x} = 2.5°\text{C}$. CO_3^{2-} concentrations were calculated as in (*14*), except K_1 and K_2 of Dickson and Millero [A. G. Dickson and F. Millero, *Deep Sea Res.* **34**, 1733 (1987)] were used. The model was run on a 2.5° grid.
17. J.-P. Gattuso, M. Frankignoulle, I. Bourge, S. Romaine, R. W. Buddemeier, *Global Planet. Change* **18**, 37 (1998).
18. H. J. Spero, J. Bijma, D. W. Lea, B. E. Bemis, *Nature* **390**, 497 (1997).
19. J. R. Ware, S. V. Smith, M. L. Reaka-Kudla, *Coral Reefs* **11**, 127 (1992).
20. We thank other members of the workshop Coral Reefs and Global Change: Adaptation, Acclimation, or Extinction (R. Bak, J. Benzie, B. Carlson, T. Done, R. Gates, B. Hatcher, R. Karlson, R. Kinzie III, R. Rowan, J. Pandolfi, A. Pittock, D. Potts, and S. Smith), sponsored by the Society for Integrative and Comparative Biology, Land Ocean Interactions in the Coastal Zone, Scientific Committee on Oceanic Research, and the National Oceanic and Atmospheric Administration.

13 October 1998; accepted 26 February 1999

Lateral Variations in Compressional/Shear Velocities at the Base of the Mantle

Michael E. Wysession,[1]* Amy Langenhorst,[2] Matthew J. Fouch,[3] Karen M. Fischer,[3] Ghassan I. Al-Eqabi,[1] Patrick J. Shore,[1] Timothy J. Clarke[4]

Observations of core-diffracted P (P_{diff}) and SH (SH_{diff}) waves recorded by the Missouri-to-Massachusetts (MOMA) seismic array show that the ratio of compressional (P) seismic velocities to horizontal shear (SH) velocities at the base of the mantle changes abruptly from beneath the mid-Pacific (V_P/V_S = 1.88, also the value predicted by reference Earth models) to beneath Alaska (V_P/V_S = 1.83). This change signifies a sudden lateral variation in material properties that may have a mineralogical or textural origin. A textural change could be a result of shear stresses induced during the arrival at the core of ancient lithosphere from the northern Pacific paleotrench.

The core-mantle boundary (CMB) is an important component of the global system of mantle convection (*1*), but direct observations of mantle flow at this depth have been frustratingly difficult to obtain (*2*). The CMB region includes a thick thermal boundary layer (labeled D''), large lateral variations at great and small scales (*3, 4*) that likely involve chemical boundary layers, an apparent discontinuous increase in seismic velocity 250 ± 100 km above the core (*5*), an ultralow-velocity zone probably attributable to partial melting (*6*), boundary topography, and seismic anisotropy (*7*). Most studies of the CMB have used observations of either *P* or *S* waves, but not both, as available energy radiation patterns and analytical techniques often differ greatly. However, the use of *P* and *S* waves simultaneously can help in identifying the state and composition of rock within Earth. Here, we present an analysis of both core-diffracted $P_{\rm diff}$ and $SH_{\rm diff}$ waves across the CMB, using earthquake sources that provide ample *P* and *SH* energy.

We sampled two regions of *D″*, beneath the northeast Pacific Ocean and beneath Alaska, that have been previously studied with *SH* and *SV* waves from western Pacific rim earthquakes traveling west-to-east to North American seismometers. Beneath Alaska the *SH* waves, oscillating north-south and perpendicular to the trend of subduction, are observed to travel up to 3% faster than *SV* waves, which vibrate vertically (*7–9*). Our data suggest 0.2 to 0.6% for the region of interest here (Fig. 1). Previously, this observation was modeled with transverse isotropy having horizontal directions that are fast relative to the vertical direction. Beneath the northeastern Pacific, however, results suggest a much more complex anisotropy (*10*). Some regions have been modeled by a complex distribution of vertically oriented laminar sheets entrained in a broad Pacific CMB upwelling (*2*), although adjacent areas are consistent with transverse isotropy. Because seismic sources are not available that can provide *SH* and *SV* waves perpendicular to these observations, we have had no constraints on the kinds of oscillations that occur east-west, along the strike of the subduction. The *P*-wave observations presented here give an additional dimension that can help resolve the structure of these two dynamically active regions of the CMB.

Core-diffracted waves can be observed over a large distance range (~100° to >150°) and can sample *D″* beneath the mid-Pacific as well as the Pacific rim, allowing us to see a transition between them (*11*). We used data from the MOMA array, which had 20 seismometers that spanned more than 1500 km (*12*). During the 15 months of the array, 58 profiles of $P_{\rm diff}$, $pP_{\rm diff}$, and $sP_{\rm diff}$ and 48 profiles of $S_{\rm diff}$ and $sS_{\rm diff}$

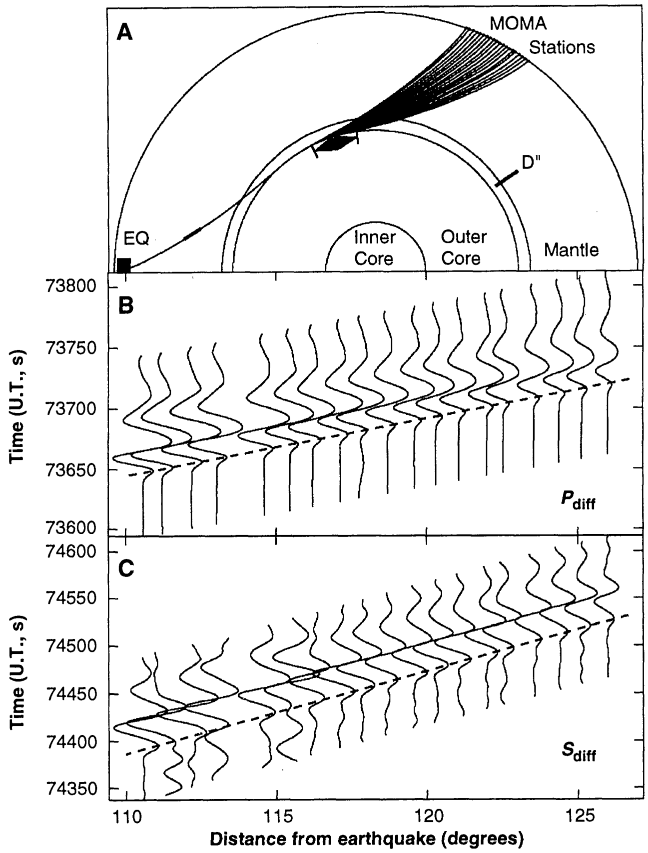

Fig. 2. (**A**) Example of the paths of core-diffracted waves recorded at the broadband seismometers of the MOMA array, in this case for $P_{\rm diff}$ waves from an earthquake in the Loyalty Islands on 16 May 1995. The downswing paths are nearly identical, but the upswing paths go through different parts of the mantle (for which we attempt to correct). The core-diffracted *P* and *S* waves ($P_{\rm diff}$ and $S_{\rm diff}$) travel nearly the same paths through the mantle, spending much time in the *D″* layer at the base of the mantle. (**B** and **C**) The waveforms of the $P_{\rm diff}$ and $S_{\rm diff}$ arrivals for this earthquake, bandpass-filtered between 0.02 and 0.04 Hz. Because all of the data bottom at the same depth (the CMB), the slownesses (or ray parameters) are straight lines that are represented on these distance-time plots as dashed lines. These slownesses, called "apparent slownesses" because the exact values vary with the technique of measurement and frequencies used, are a function of the mean velocity at the base of the mantle. The waves all travel a long distance across *D″*; the slowness measures the velocities in the region between the CMB exit points of the nearest and furthest seismometers, shown in (A) by the arrowheads. For this earthquake the total distance range is 15.4° (110.5° to 125.9°), corresponding to 1710 km at the surface and 935 km at the CMB. There is a trade-off in the desired array length, as shorter distances make the slowness more susceptible to travel-time errors due to noise and mantle heterogeneity along the different mantle upswing paths, but longer array lengths give a slowness that may average over regions of smaller scale CMB variations. We used a bandpass filter of 0.02 to 0.04 Hz to avoid geometric dispersion of $P_{\rm diff}$ and $S_{\rm diff}$, which occurs because different wavelengths sample different depths into the mantle and therefore travel at different velocities (*28*). Our earthquakes occur at different magnitudes and thus have peak energies at different frequencies, resulting in a possible source of bias if they are not uniformly bandpass-filtered. We corrected the arrival times for ellipticity, mantle path heterogeneity, and upper-mantle anisotropy (*29*), and determined the apparent slowness with a least squares fit through the pulse peak maxima times (*30*).

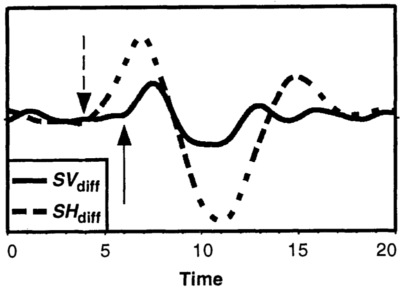

Fig. 1. An example of $SH_{\rm diff}$ and $SV_{\rm diff}$ waveforms that sample the CMB beneath Alaska, verifying previous results (*7–9*) that show this region to have faster V_{SH} than V_{SV} (*24*). Only one earthquake (Marianas, 23 August 1995, depth 595 km) provided good $SH_{\rm diff}$ and $SV_{\rm diff}$ data to examine the *D″* shear-wave splitting in this region. All clearly split arrivals show V_{SH} faster than V_{SV}, and the degree of splitting suggests a regional anisotropy of 0.2 to 0.6%, assuming that the anisotropy is uniformly distributed along the *D″* segment of each path. In this example, for station MM06 in Emporium, PA, $SH_{\rm diff}$ (dashed line) arrives about 2 s earlier than $SV_{\rm diff}$ (solid line). The waveforms, bandpass-filtered at 2 to 60 s, have been corrected for particle motion perturbations resulting from upper-mantle anisotropy beneath the stations (*26*). The arrows pointing to the phase arrivals are for demonstration only, as splitting in the $S_{\rm diff}$ phases was calculated using a new, more reliable "master station" method (*24*). A master station with particularly clear $SV_{\rm diff}$ and $SH_{\rm diff}$ arrivals was selected for each event. After normalizing instrument responses for all stations, individual $SV_{\rm diff}$ and $SH_{\rm diff}$ waveforms from each station were cross-correlated with the respective master station $SV_{\rm diff}$ and $SH_{\rm diff}$ waveforms to determine relative arrival times with 95% *F*-test confidence limits. Splitting at each station was obtained by combining its relative times with splitting at the master station. This method provides a rigorous and quantitative approach to determining $S_{\rm diff}$ splitting, because it produces an accurate and objective measurement of splitting in phases with ambiguous onset times, provides better estimation of errors, and enables the evaluation of waveforms with lower signal-to-noise ratios.

---

[1]Department of Earth and Planetary Sciences, Washington University, St. Louis, MO 63130, USA. [2]Department of Geological Sciences, Northwestern University, Evanston, IL 60208, USA. [3]Department of Geological Sciences, Brown University, Providence, RI 02912, USA. [4]Department of Earth and Environmental Science, New Mexico Institute of Mining and Technology, Socorro, NM 87801, USA.

*To whom correspondence should be addressed. E-mail: michael@wucore.wustl.edu

were obtained. Both P_{diff} and S_{diff} were obtained for 36 of these array profiles.

We used the slowness, or ray parameter, of the diffracted waves across the seismic array (Fig. 2) to estimate the mean velocity at the base of the mantle, and we combined all the arrivals across the array from any one earthquake to obtain a single measurement. Corrections were made for mid- and upper-mantle path anomalies, Earth's ellipticity, and upper-mantle anisotropy beneath North America to isolate the seismic velocities at the base of the

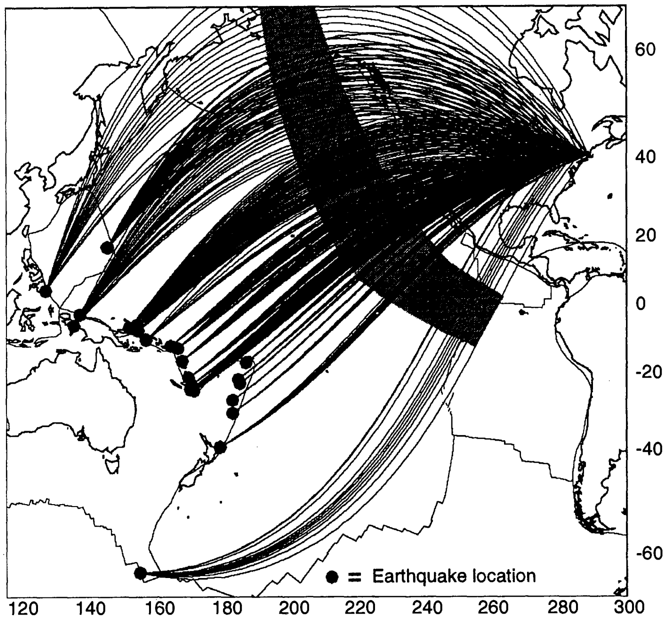

Fig. 3. Map showing the paths for earthquakes that had high-quality P_{diff} and S_{diff} arrivals at MOMA. A total of 36 different sets of paths (profiles) are used from 30 different earthquakes (30 pairs of P_{diff} and S_{diff} and six pairs of surface-reflected pP_{diff} and sS_{diff} are used). Circles are the locations of earthquakes, and the dark shaded region is the part of the CMB that is measured by the MOMA profile slownesses. For paths that arrive exactly parallel to the array, such as from the Kermadec Trench, the full 15.6° distance range of the MOMA stations is spanned by the arrivals. The shortest distance range (123.3° to 128.5°) was for a Philippines earthquake, which also had the largest azimuthal range (17.3° to 35.6°). The slowness of the latter (relative to the Kermadec profiles) is about three times as susceptible to errors due to upper-mantle heterogeneity, but because the same paths are sampled by both P and S waves, the V_P/V_S ratio will still be reliable. The three-dimensional V_P and V_S mantle models we used to correct the differential mantle paths have been shown to correlate well with each other in the mid- and upper mantles beneath North America, where our ray paths are the most divergent (*3*, *4*). We calculate that the uncertainties in the slownesses are 0.3% for the along-axis paths and 1.0% for the furthest off-axis paths.

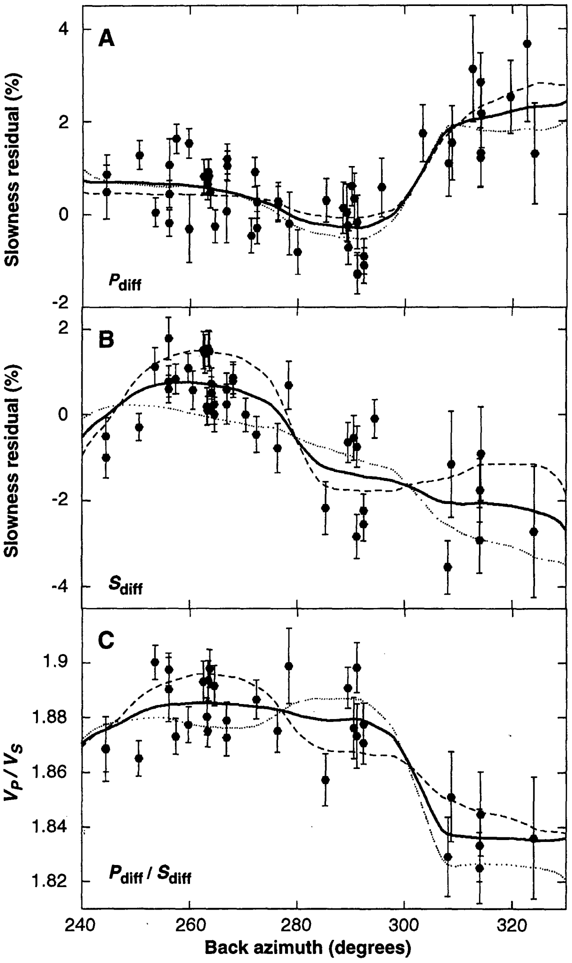

Fig. 4. (**A**) Plot of the P_{diff} slowness residuals as a function of mean back azimuth at the recording MOMA stations. The span of the back azimuths corresponds to the span of the shaded region in Fig. 3, with the highest back azimuths (>300°) corresponding to the region of the CMB beneath Alaska and the northern rim of the Pacific Ocean. Slowness residuals represent a percentage variation from PREM (*25*), obtained by taking the apparent slowness of the data and subtracting out slowness values found from synthetic waveforms that are processed in the same manner. Although a radially symmetric Earth model is used for the synthetics, the synthetic slownesses varied because of differences in focal mechanism radiation amplitudes and shifting waveforms for differing station distances. The mean of the synthetic slownesses is 4.58 s per degree, but the range is 4.52 to 4.75 s per degree, so even though the data slownesses have already been corrected for anisotropy, mantle path heterogeneity, and upper-mantle anisotropy, it is important to work with slowness residuals as opposed to the observed apparent slownesses themselves. The time-corrected data slownesses have a mean of 4.60 ± 0.07 s per degree (range, 4.41 to 4.90 s per degree). The solid line represents a moving average across the residuals with a window of 16°. The residuals show a 5% variation, but the smoothed curve spans 2.5%. The slowness residuals are decidedly different at the northern paths, with back azimuths of >300°, suggesting D'' velocities that are much slower than normal. Reliability is shown in two ways. The error bars on all of the slowness values show the 1σ variation in the linear regression results assuming a standard variation of 0.5 s in the travel times. Also shown are the equivalents of the moving average (solid line) if the entire analysis were repeated with no travel-time corrections (dashed line) and with travel-time corrections doubled (dotted line). (**B**) Same as above but for S_{diff} slowness residuals. The time-corrected data slownesses have a mean of 8.47 ± 0.13 s per degree and a range of 8.21 to 8.73 s per degree. The synthetic slownesses have a mean of 8.49 s per degree (range, 8.40 to 8.85 s per degree). The slowness residuals have nearly a 6% range, but the smoothed curve shows a 3% variation. The lowest slowness values, and therefore the fastest D'' velocities, are found beneath the northern Pacific and Alaska. (**C**) Plot of the V_P/V_S ratios for rock at the base of the mantle sampled by the P_{diff} and S_{diff} profiles. The ratios are computed from the slowness residuals using conversions obtained with synthetic modeling (*27*). Moving south to north along the CMB (MOMA back azimuth 250° to 295°), we see that the V_P/V_S ratio is about constant at 1.88 as both P and S velocities are increasing, likely an effect of decreasing temperatures as the paleoslab graveyard is approached. However, for the northernmost region at the CMB (back azimuth > 300°), there is a sudden change in V_P/V_S, likely the result of mineralogical or textural anisotropy.

mantle, and slownesses were interpreted relative to synthetic seismograms computed for a reference Earth and the same earthquake-station geometries. The resulting *P* and *S* velocities at the CMB extend along a swath that extends beneath the northeastern Pacific at a distance of ~50° from the array (Fig. 3).

The total slowness variations are 2% for P_{diff} and 3% for S_{diff} (roughly the same for inferred velocity variations) (Fig. 4, A and B). The *P* velocities are slightly slow at the CMB beneath the eastern Pacific and gradually equal globally averaged values toward the northwest (back azimuth = 240° to 320°), where they abruptly become very slow (back azimuth > 300°). The *SH* velocities are slow at the CMB west of Mexico (back azimuth ≈ 260°) but become increasingly faster toward the northwest. The *SH* velocities are also fast for the very southernmost region (back azimuth < 250°), which is not unusual, as this region of D'' is east of the large mid-Pacific slow-velocity anomalies observed in many studies. For back azimuth < 300° (CMB south of 40°N) the ratio of *P* to *S* velocities, V_P/V_S, ranges between 1.86 and 1.90, with the scatter likely a result of the complex D'' anisotropy observed beneath the Pacific. However, this ratio drops sharply to about 1.83 for the northernmost CMB region beneath Alaska and the northernmost Pacific (Figs. 4C and 5). This drop corresponds to a reduction in the ratio of *P* to *SH* velocities $(V_P/V_S)_2/(V_P/V_S)_1$ of 2.7%. This kind of anticorrelation between *P* and *SH* velocities is rare within Earth, but has previously been observed for D'' (*13*).

Reference Earth models predict V_P/V_S values of 1.88 to 1.89 for the base of the mantle (*14*), which is what we find in the region beneath the northeastern Pacific. The effect of anisotropy in this region, which is observed to be highly variable over short spatial scales (*2, 10*), either is averaged out or is the same for *SH* and *P*. However, relative to reference models, the D'' layer beneath Alaska is anomalous and is consistent with results from previous *P*- and *S*-wave mantle tomographic models: D'' velocities beneath Alaska are faster than average for *S* and slower than average for *P* (*15*). The data for the tomographic models incorporate different seismic phases but share the same characteristic in that their paths predominantly travel west-east and east-west, parallel to the subduction axis.

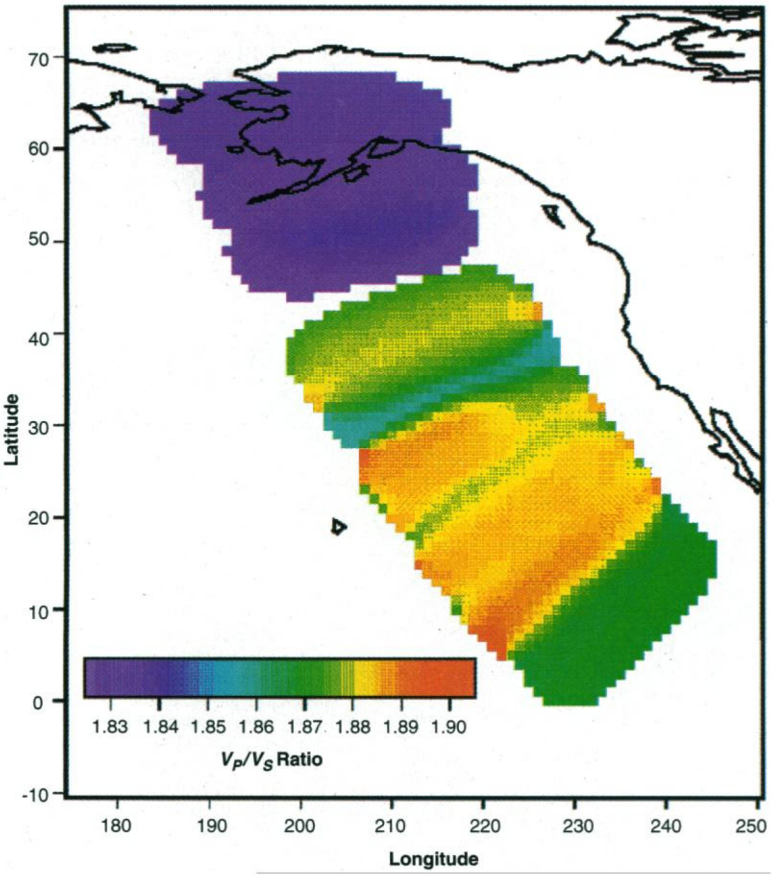

Fig. 5. Map showing the inferred variations in V_P/V_S found from the combination of the P_{diff} and S_{diff} slowness residuals. Values are found by projecting the V_P/V_S anomalies along the mean sampling paths for the P_{diff} and S_{diff} profiles, and then smoothing them by averaging with a 5° moving Gaussian cap (*31*). Although most of the CMB beneath the northeastern Pacific has V_P/V_S values between 1.87 and 1.89, expected from global seismic models, the northernmost region drops suddenly to 1.83. Such a reduction is not likely to happen as a result of temperature effects alone; it requires a change in material property, either as an unusual chemical anomaly or (more likely) as an occurrence of azimuthal anisotropy. The location of this anomaly correlates with the region of the CMB projected to receive the greatest amount of postsubduction paleoslab (*16*), so any resulting azimuthal anisotropy would be an indication of advective flow at the CMB of the proposed paleoslab material.

The challenge is to understand the geophysical processes that cause this *P*/*SH* anticorrelation, which likely involve the sinking of subducted lithosphere to the CMB. Recent mantle tomographic models show subducted slabs penetrating deep into the lower mantle, and it is thought that there is a large amount of paleoslab material arriving at the CMB in this region (*16*). We would expect that this paleoslab would be colder than ambient D'' temperatures, and that it may have slight bulk chemical differences with respect to the lowermost mantle. The change in temperature should not by itself cause the V_P/V_S anomaly: V_P and V_S generally increase or decrease together in the presence of temperature variations. However, it is possible that the ambient D'' layer could contain a small amount of partial melt that depresses V_S values everywhere except in regions of cold downwellings (*17*). *P* velocities would be less affected by the presence of melt, and it is the P_{diff} slownesses that show the greatest change across our regions of sampling. This still would not explain the differences between *SH* and *SV* velocities observed in D'' beneath Alaska.

One possibility is chemical heterogeneity, which can affect the bulk and shear moduli, K_S and μ, differently such that V_P and V_S are anticorrelated (*18*). A decoupled D'' chemical boundary layer is likely to be thinnest beneath regions of downwelling [this is observed for the ultralow-velocity zone at the base of D'' (*6*)], but thicker beneath upwellings. In this case, the V_P/V_S ratio of 1.83 beneath Alaska is representative of the anomalous paleoslab rock, and the V_P/V_S ratio of 1.88 beneath the Pacific is for the chemical boundary layer, which covers the majority of the CMB and is therefore obtained by global reference models. Many studies observe much larger *S*-velocity anomalies at the base of the mantle than *P*-velocity anomalies, and this has often been ascribed to temperature effects due to the presence of a large thermal boundary layer. In the scenario just presented, however, the lateral velocity variations would be due to chemical variations. The northern part of our sample region, beneath Alaska, would appear to be "anomalous" in the sense that it is similar to the overlying mantle and therefore different from the D'' chemical boundary layer.

Another candidate for explaining the anticorrelation of V_P and V_{SH} in D'' is that of preferentially oriented textural fabric: Our P_{diff} waves are slow because they are traveling in a slow direction. The model of transverse isotropy used by (*19*) to explain *SH*/*SV* splitting involves the horizontal layering of low-velocity material within a faster matrix (such as former ocean crust within the cold paleoslab). As this cannot explain our slow P_{diff} waves, such a model would need to be accompanied by either the chemical heterogeneity mentioned above or a mineralogical anisotropy. Our calculations show that other orientations of D'' rock fabric might provide a shape-preferred orientation (SPO) style of anisotropy that explains our seismic constraints: (i) transverse isotropy with fast inclusions and (ii) azimuthal anisotropy with either fast or slow cigar-shaped inclusions oriented perpendicular to the paleotrench (*20*). The latter is especially attractive in light of recent evidence that areas previously modeled with transverse isotropy, like D'' beneath the Caribbean, are now suggesting azimuthal or general anisotropy (*21*).

Minerals such as perovskite, periclase, and columbite-structured silica are highly anisotropic at CMB conditions, and they have orientations in which *SH* is fast and *SV* and *P* are slow (*9*, *22*). Although none of these currently match our seismic anomalies under the condition of lateral flow at the CMB away from the paleotrench, there is a suggestion that the high-pressure transition from diffusion creep to dislocation glide would change the expected mineralogical glide planes (*23*), so mineralogical anisotropy with a lattice-preferred orientation (LPO) remains a candidate.

As a result, the model of transverse isotropy due to horizontal layering is still a possible candidate for the seismic structure of D'' beneath the Alaska paleotrench, though a modification is required to satisfy the unusually slow P_{diff} velocities we observe. One possibility is that the flow of paleoslab rock causes anisotropy, either LPO or SPO in origin, that has a slow *P*-velocity direction along the strike of the paleotrench. Another is that, assuming the slower *P* velocities are typical of paleoslab rock, there is a large chemical difference between paleoslab and a chemical boundary layer that is thicker away from the paleotrench, and this chemical boundary layer dominates in global reference models. In any case, there is a material difference between rock at the base of the mantle beneath the interior and at the northern rim of the Pacific Ocean.

References and Notes

1. T. H. Jordan, *Proc. Natl. Acad. Sci. U.S.A.* **76**, 4192 (1979); G. F. Davies and M. Gurnis, *Geophys. Res. Lett.* **13**, 1517 (1986).
2. T. Lay, Q. Williams, E. J. Garnero, *Nature* **392**, 461 (1998).
3. R. D. van der Hilst, S. Widiyantoro, E. R. Engdahl, *Nature* **386**, 578 (1997).
4. S. P. Grand, R. D. van der Hilst, S. Widiyantoro, *GSA Today* **7**, 1 (1997).
5. M. E. Wysession *et al.*, in *The Core-Mantle Boundary Region*, M. Gurnis, M. E. Wysession, E. Knittle, B. A. Buffett, Eds. (American Geophysical Union, Washington, DC, 1998), pp. 273–297.
6. E. J. Garnero, J. Revenaugh, Q. Williams, T. Lay, L. H. Kellogg, *ibid.*, pp. 319–334.
7. T. Lay, E. J. Garnero, Q. Williams, L. Kellogg, M. E. Wysession, *ibid.*, pp. 299–318; E. J. Garnero and T. Lay, *J. Geophys. Res.* **102**, 8121 (1997).
8. E. Matzel, M. K. Sen, S. P. Grand, *Geophys. Res. Lett.* **23**, 2417 (1996).
9. J.-M. Kendall and P. G. Silver, in (*5*), pp. 97–118.
10. Relative to *SV*, observed *SH* velocities have been either fast (*24*) [L. P. Vinnik, V. Farra, B. Romanowicz, *Bull. Seismol. Soc. Am.* **79**, 1542 (1989); L. Vinnik, B. Romanowicz, Y. Le Stunff, L. Makeyeva, *Geophys. Res. Lett.* **22**, 1657 (1995)], slow [J. Pulliam and M. K. Sen, *Geophys. J. Int.* **135**, 113 (1998)], the same (*9*), or variable at small to intermediate spatial scales (*24*) [L. Vinnik, L. Bregér, B. Romanowicz, *Nature* **393**, 564 (1998); S. A. Russell, T. Lay, E. J. Garnero, *ibid.* **396**, 255 (1999)].
11. R. W. Valenzuela and M. E. Wysession, in (*5*), pp. 57–71.
12. The MOMA Broadband Deployment involved the temporary installation of 18 broadband-frequency seismic sensors in a linear array between permanent stations CCM (Cathedral Caves, MO) and HRV (Harvard, MA). Instruments were borrowed from the PASSCAL program of the Incorporated Research Institutions for Seismology (IRIS), and data were recorded between January 1995 and April 1996. The location was chosen because it records on average more than half (53%) of large global earthquakes in the range 100° to 140°, and as such it is ideal for the detection of core-diffracted waves [M. E. Wysession *et al.*, *Eos* **77**, 477 (1996)]. MOMA was unusual for seismic arrays in that it was largely designed for the purpose of examining structure at the base of the mantle.
13. M. E. Wysession, E. A. Okal, C. R. Bina, *J. Geophys. Res.* **97**, 8749 (1992); G. S. Robertson and J. H. Woodhouse, *ibid.* **101**, 20041 (1996); H. Bolton and G. Masters, *Eos* **77**, F697 (1996).
14. The V_P/V_S ratios across the bottom 250 km of the mantle are 1.888 to 1.878 for the Preliminary Reference Earth Model (PREM) (*25*) and 1.875 to 1.876 for the Iasp91 model [B. L. N. Kennett and E. R. Engdahl, *Geophys. J. Int.* **105**, 429 (1991)].
15. For *P*-velocity models with slower than average D'' velocities beneath the northernmost Pacific and Alaska, see (*3*); H. Inoue, Y. Fukao, K. Tanabe, Y. Ogata, *Phys. Earth Planet. Inter.* **59**, 294 (1990); R. J. Pulliam, D. W. Vasco, L. R. Johnson, *J. Geophys. Res.* **98**, 699 (1993); M. E. Wysession, *Nature* **382**, 244 (1996). For *S*-velocity models with faster than average D'' velocities beneath the northernmost Pacific and Alaska, see (*4*); T. Tanimoto, *Geophys. J. Int.* **100**, 327 (1990); W. Su, R. L. Woodward, A. M. Dziewonski, *J. Geophys. Res.* **99**, 6945 (1994); G. Masters, S. Johnson, G. Laske, H. Bolton, *Philos. Trans. R. Soc. London Ser. A* **354**, 1385 (1996); X.-D. Li and B. Romanowicz, *J. Geophys. Res.* **101**, 22245 (1996); M. Sylvander and A. Souriau, *Phys. Earth Planet. Inter.* **94**, 1 (1996); A. M. Dziewonski, G. Ekström, X.-F. Liu, in *Monitoring a Comprehensive Test Ban Treaty* (Kluwer Academic, Dordrecht, Netherlands, 1996), pp. 521–550; B. Y. Kuo and K. Y. Wu, *J. Geophys. Res.* **102**, 11775 (1997).
16. Y. Ricard, M. A. Richards, C. Lithgow-Bertelloni, Y. Le Stunff, *J. Geophys. Res.* **98**, 21895 (1993); C. Lithgow-Bertelloni and M. A. Richards, *Rev. Geophys.* **36**, 27 (1998).
17. Melt may accumulate at the base of the mantle because it may have a greater density than surrounding solids [S. M. Rigden, T. J. Ahrens, E. M. Stolper, *J. Geophys. Res.* **94**, 9508 (1989)], especially if iron partitions preferentially into the liquid [E. McFarlane, M. J. Drake, D. C. Rubie, *Geochim. Cosmochim. Acta* **58**, 5161 (1994); E. Ohtani, T. Kato, E. Ito, *Geophys. Res. Lett.* **18**, 85 (1991)].
18. M. E. Wysession, C. R. Bina, E. A. Okal, in *Dynamics of the Earth's Deep Interior and Earth Rotation*, J.-L. LeMoüel *et al.*, Eds. (American Geophysical Union, Washington, DC, 1993), pp. 181–190.
19. J.-M. Kendall and P. G. Silver, *Nature* **381**, 409 (1996).
20. Using the formulation of G. P. Tandon and G. J. Weng [*Polym. Composites* **5**, 327 (1984)] in an analysis similar to that of (*9*) and (*19*), we found that two different classes of heterogeneous inclusions could provide 0.5% anisotropy for V_{SH} versus V_{SV} and 2.7% for V_{SH} versus V_P without altering the matrix composition: (i) horizontal sheets of anomalously fast material (transverse isotropy), and (ii) horizontal cigar-shaped inclusions oriented perpendicular to the direction of propagation (north-south, perpendicular to the paleotrench). For an example of the horizontal sheets, if the inclusions have *S* velocities that are increased by 11% over a pyrolite composition at CMB temperature and pressure (which has $K_S = 601$ and $\mu = 337$) and *P* velocities that are increased by 5% (most of the increase is in the shear modulus), then the sheets would need to occupy 30% of the rock volume. All of the velocities, including V_P, would increase relative to ambient conditions, so an additional factor would have to reduce all velocities for V_P to be slower than the global average. The inclusion of seismically slow sheets cannot explain the V_{SH} versus V_P difference without overestimating the V_{SH} versus V_{SH} anisotropy unless the D'' matrix is chemically different from that beneath the mid-Pacific. The cigar-shaped inclusions, taken here to have a 20-to-1 aspect ratio, may be either fast or slow to explain the anisotropy. Elongated tubules could have either $\Delta V_S = +50\%$ and $\Delta V_P = +32\%$ occupying 13% of the rock volume, or $\Delta V_S = -25\%$ and $\Delta V_P = -30\%$ with a volume of 24%. Elongated anomalies might result from the lateral shearing of D'' beneath the more viscous lower mantle, though the inclusion volumes and velocity differences are extremely large. With the fast-velocity tubules, all velocities are increased, and a mechanism (most likely chemical) is required to lower them all so that the *P* velocities are slower than the global average. With the slow-velocity tubules, all velocities are decreased, so a mechanism (most likely thermal) is required to make the *S* velocities faster than the global average.
21. T. Lay, E. J. Garnero, V. Maupin, *Eos* **79**, F607 (1998).
22. L. Stixrude, in (*5*), pp. 83–96; S. I. Karato, S. Zhang, H. R. Wenk, *Science* **270**, 458 (1995).
23. S. Karato *et al.*, *Eos* **79**, F607 (1998).
24. M. J. Fouch, K. M. Fischer, M. E. Wysession, *ibid.*, p. F617.
25. A. M. Dziewonski and D. L. Anderson, *Phys. Earth Planet. Inter.* **25**, 297 (1981).
26. M. J. Fouch, K. M. Fischer, M. E. Wysession, T. J. Clarke, in preparation.
27. A. H. Mula and G. Müller, *Pure Appl. Geophys.* **118**, 1270 (1980).
28. E. A. Okal and R. J. Geller, *Bull. Seismol. Soc. Am.* **69**, 1039 (1979).
29. Ellipticity corrections were made according to H. Jeffreys and K. E. Bullen [*Seismological Tables* (British Association for the Advancement of Science, London, 1970)]. Travel-time corrections were made for mantle paths outside of the region of D'' sampled by tracing the ray paths through whole-mantle tomographic models separately for *P* velocities (*3*) and *S* velocities (*4*). Corrections for receiver-side mantle anisotropy above D'' were made using shear-wave splitting parameters determined from *SKS* and *SKKS* waves recorded at MOMA (*26*). To estimate S_{diff} polarizations exiting the CMB, we measured amplitudes of SH_{diff} and SV_{diff} at the nearest stations for each earthquake; these were predicted at more distant stations with the use of theoretical amplitude decay constants [D. J. Doornbos and J. C. Mondt, *Geophys. J. R. Astron. Soc.* **57**, 353 (1979)], as SV_{diff} energy decays rapidly around the CMB and waveforms are often lost in the codae of *SKKS* arrivals. Synthetic time offsets for SH_{diff} were then obtained by computing how an S_{diff} phase with the appropriate polarization would be split by shallower mantle anisotropy with the orientation and magnitude inferred from the *SKS* and *SKKS* phases. Although the estimated S_{diff} polarizations can only approximate actual S_{diff} polarizations as they exit the core, the SH_{diff} time corrections are relatively insensitive to reasonable S_{diff} polarization errors. In addition, although the assumption that splitting in *SKS*/*SKKS* phases reflects anisotropy above D'' may not be entirely accurate if azimuthal anisotropy exists in D'' beneath the eastern United States, D'' contributions to *SKS*/*SKKS* splitting appear to be small if they exist at all. Predicted time shifts in P_{diff} phases due to receiver-side mantle anisotropy above D'' are small, and time corrections for this effect are not applied to the data.
30. Selecting onset arrival times, common for most other

seismic phases, is not possible for core-diffracted waves because of the rapid loss of high frequencies during diffraction. A linear regression through the times of the wave peak maxima is the common means of determining the apparent slowness (*18, 27*) [J. C. Mondt, *Phys. Earth Planet. Inter.* **15**, 46 (1977); A. Souriau and G. Poupinet, *ibid.* **84**, 227 (1994)], and this has been shown to be as reliable as using a multiwaveform cross-correlation [M. E. Wysession and E. A. Okal, *Geophys. Res. Lett.* **16**, 1417 (1989)].

31. M. E. Wysession, L. Bartkó, J. Wilson, *J. Geophys. Res.* **99**, 13667 (1994).
32. We thank the many people with the IRIS PASSCAL and DMC programs who helped with the MOMA experiment and K. Koper, A. Li, E. Roth, L. Salvati, R. Valenzuela, and J. Zaslow for additional help with the MOMA deployment. Supported by NSF grants EAR-9319324, EAR-9315971, and EAR-9315925 and by the David and Lucile Packard Foundation.

14 October 1998; accepted 23 February 1999

High-Resolution Holocene Environmental Changes in the Thar Desert, Northwestern India

Y. Enzel,[1] L. L. Ely,[2] S. Mishra,[3] R. Ramesh,[4] R. Amit,[5] B. Lazar,[1] S. N. Rajaguru,[3] V. R. Baker,[6] A. Sandler[5]

Sediments from Lunkaransar dry lake in northwestern India reveal regional water table and lake level fluctuations over decades to centuries during the Holocene that are attributed to changes in the southwestern Indian monsoon rains. The lake levels were very shallow and fluctuated often in the early Holocene and then rose abruptly around 6300 carbon-14 years before the present (^{14}C yr B.P.). The lake completely desiccated around 4800 ^{14}C yr B.P. The end of this 1500-year wet period coincided with a period of intense dune destabilization. The major Harrapan-Indus civilization began and flourished in this region 1000 years after desiccation of the lake during arid climate and was not synchronous with the lacustral phase.

The southwestern Indian monsoon is critical for understanding past global and regional monsoon variations (*1–3*). The few records of Holocene monsoon variations from the areas that border the Arabian Sea in southern Asia have been based on pollen assemblages associated with the deposits of Lunkaransar, Didwana, and Sambhar paleolakes from northwestern India (*4*). These records, although based on limited dating, have been used extensively in regional compilations, in analysis of relations between summer insolation and the monsoon, and in paleoclimatic models (*2–7*) as well as to determine the relations between paleoclimate and Indus Valley civilizations (*8, 9*). Here, we present more detailed Holocene chronology of Lunkaransar based on analyses of the lacustrine laminated deposits, age dating, and geochemical analyses.

Lunkaransar (*10*) is a small, closed, dry basin surrounded by dunes at the northeastern margin of the Thar Desert (Fig. 1). The basin receives input from groundwater and direct rain and no input from streams. The water table is currently 2.4 m below the dry lake bed, and this water is saline with a composition that includes Na, Ca, Mg, Cl, SO_4, and HCO_3. Incoming sediments are only eolian sand from local dunes and eolian clay silt dust (*11*). Normally, the lake basin is totally dry, but heavy rainfall can form a temporary pool of water that evaporates during the dry season.

Trenches were excavated into the lake bed down to a thick, hard, carbonate layer at a depth of 3 m. The sedimentology of the upper 240 cm above the water table (Fig. 2) was documented at submillimeter-to-millimeter scales in both the field exposures and in the continuous, overlapping box cores in the laboratory. We obtained 15 radiocarbon dates (Table 1). The sequence was divided into four zones (Fig. 2) on the basis of characteristics of the deposits. Zone 4, dated at 4800 ^{14}C yr B.P. to recent, has no primary laminar structure and contains mud cracks, silt, and sand; it is interpreted as a dry lake basin that episodically was inundated by ephemeral lakes. Zones 1 to 3 (Figs. 2 and 3) are composed of two types of thin beds: (i) silt- and clay-rich detritus laminae with carbonate and in some cases thin gypsum laminae at boundaries, and (ii) gypsum laminae with some thin silt and clay laminae. We separated the entire sequence into four sedimentary facies (II to V) according to the dominant type and the thickness of the various beds (Fig. 3E) and inferred relative water depths

Field observations show that the maximum lake stage did not reach 5 to 7 m. The ability of the basin to sustain even this level (facies IV and V) through successive years varied significantly throughout the Holocene (Fig. 3E).

Thin-section and x-ray diffraction analyses indicate that the clastics are allochthonous silicate minerals (quartz, plagioclase, potassium feldspar, clays such as chlorite and mica, and some hornblende), carbonate minerals, and some gypsum. Gypsum is the only evaporite mineral detected. The clay fraction (<2 μm) includes illite-smectite, illite, chlorite, and palygorskite. The palygorskite is authigenic and is indicative of intense evaporation episodes (*12*) at pH $\approx$ 8.5.

The concentration of clastic grains in separate laminae and the parallel orientation of the platy and elongated minerals indicate that the clastic grains were derived from dust storms (*11*) and they settled in water. The gypsum laminae contain fine authigenic crystals and abraded, sand-sized gypsum crystals. The abraded gypsum grains are most common in facies II and were probably blown in from drying mudflats at the margins (*13*) of Lunkaransar lake during periods of low lake levels.

The rise and fall of the water table at Lunkaransar reflect the regional precipitation over the basin. A lake is formed in Lunkaransar when the water table rises above the surface. Our data show that between about

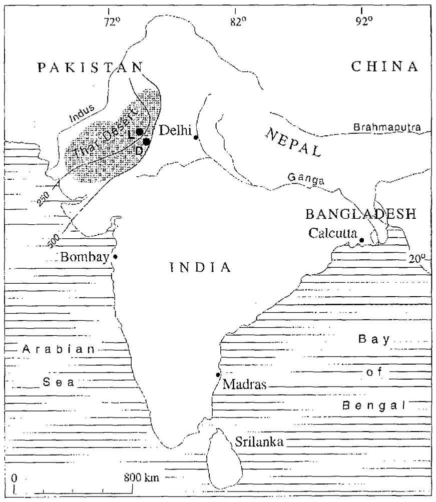

Fig. 1. Location map of Lunkaransar (L) and Didwana (D) dry lakes in the Thar Desert (shaded area) showing 250- and 500-mm/year isohyets.

---

[1] Institute of Earth Sciences and Department of Geography, The Hebrew University of Jerusalem, Jerusalem 91904, Israel. [2] Department of Geology, Central Washington University, Ellensburg, WA 98926, USA. [3] Deccan College, Deccan College Road, Pune 411006, India. [4] Earth Science Division, Physical Research Laboratory, Ahmedabad 380009, India. [5] Geological Survey of Israel, 30 Malkhei Israel Street, Jerusalem, Israel. [6] Department of Hydrology and Water Resources, University of Arizona, Tucson, AZ 85721, USA.